

Research article

Pb-free metal oxide-based epoxy resin nanocomposites for radiation protection: Physical evaluation analysis approach

Toni Beth Guatato-Lopez^{a,c,*}, Alvie Asuncion-Astronomo^b, Gil Nonato C. Santos^a

^a Department of Physics, College of Science, De La Salle University, Philippines

^b Department of Science and Technology – Philippine Nuclear Research Institute, Philippines

^c Department of Science and Technology – Central Office, Philippines

ARTICLE INFO

Keywords:

Metal oxide

Epoxy resin

Nanocomposite

Radiation protection efficiency

Mid-energy radiation

ABSTRACT

Exposure to mid-energy radiation poses significant health risks, necessitating the development of effective shielding materials. Traditional lead-based shields, while effective, have significant drawbacks including toxicity and environmental concerns. This study investigates the potential of lead-free epoxy resin nanocomposites, incorporating bismuth oxide, nickel oxide, and cerium oxide, for mid-energy radiation protection. Nanocomposites were fabricated using an open mold casting technique, and their physical properties were characterized via scanning electron microscopy (SEM) and energy dispersive X-ray (EDX) analyses. Further morphological analysis was conducted using a compound microscope and image processing software, ImageJ, to investigate the distribution of the particles on the polymer matrix. The radiation shielding effectiveness of the composites was evaluated using Na-22, Cs-137, and Mn-54 gamma sources in a gamma spectroscopy setup in Philippine Nuclear Research Institute. The results revealed that pure epoxy resin exhibited higher attenuation coefficients compared to the modified composites, primarily due to the challenges in achieving uniform dispersion of metal oxides within the polymer matrix. Agglomeration of nickel oxide nanoparticles was particularly noted, leading to reduced shielding performance. Average mass attenuation coefficients obtained in this experimental setup reached up to 0.08-0.1 cm²/g for energy range 500-900 keV. Radiation protection efficiency (RPE) measurements indicated that pure epoxy resin achieved an RPE of approximately 6% across different sources, highlighting its potential for practical applications in medical imaging, industrial radiography, environmental monitoring, and nuclear power plants. This study underscores the importance of nanoparticle dispersion and provides insights into the development of lightweight, lead-free, and efficient radiation shielding materials. Future work should focus on optimizing synthesis methods to improve homogeneity and radiation protection efficacy of polymer-based composites.

1. Introduction

Exposure to x-rays and mid-energy radiation poses significant health risks, primarily due to the generation of reactive oxygen species (ROS) and free radicals within cells, resulting in DNA damage and cellular dysfunction [1,2]. The vulnerability of cells varies,

* Corresponding author.

E-mail addresses: toni.lopez@dlsu.edu.ph, tblopez@mirdc.dost.gov.ph (T.B. Guatato-Lopez).

<https://doi.org/10.1016/j.heliyon.2024.e41394>

Received 18 June 2024; Received in revised form 19 December 2024; Accepted 19 December 2024

with highly proliferative ones such as those in the bone marrow and gastrointestinal tract being particularly susceptible [3,4]. Long-term exposure increases the risk of cancer, contributing to an estimated 100,000 cancer deaths annually worldwide [5–7]. The need for effective radiation protection is underscored by medical radiation being the largest man-made source of radiation exposure.

Lead has historically served as a primary material for radiation shielding in various fields such as medicine, industry, and plant setups due to its high density and effectiveness in attenuating gamma rays and x-rays [8]. However, lead possesses several drawbacks, including low flexibility, heaviness, and stability issues [9], as well as environmental and health hazards associated with its use and disposal [10]. Occupational exposure to lead can result in adverse health effects such as neurological impairment, kidney damage, and reproductive toxicity [11]. Furthermore, lead mining, processing, and recycling contribute to environmental pollution and pose risks to human health [12]. These concerns highlight the urgent need for alternative materials with comparable shielding efficacy but without the associated health and environmental hazards.

Polymer-based composites have garnered significant attention as promising materials for radiation shielding due to their lightweight nature, flexibility, and ease of fabrication [13–16]. Compared to traditional lead-based materials, polymer composites offer reduced toxicity, improved mechanical properties, and enhanced compatibility with additive manufacturing techniques [17]. The incorporation of high-density fillers such as bismuth oxide (Bi_2O_3), nickel oxide (NiO), and cerium oxide (CeO_2) into polymer matrices further enhances their radiation shielding effectiveness [13,18,19]. Bismuth oxide, known for its high atomic number and excellent attenuation properties against gamma rays and x-rays, has garnered particular interest [20]. Similarly, nickel oxide and cerium oxide offer promising radiation shielding capabilities while maintaining desirable mechanical and thermal properties [18,19]. By harnessing the synergistic effects of polymer matrices and high-density fillers, polymer-based composites represent a viable solution for radiation shielding across various industries, including healthcare, aerospace, and nuclear power.

In this study, we aimed to develop lead-free, high efficiency shielding materials for gamma radiation by incorporating bismuth oxide, nickel oxide, and cerium oxide into an epoxy resin polymer matrix. Morphological and elemental analyses were conducted using Scanning Electron Microscopy and Energy Dispersive X-ray techniques. To evaluate the shielding effectiveness of the composites, experimental data obtained using Na-22, Cs-137, and Mn-54 gamma sources in gamma spectroscopy setup. The findings of this study provide valuable insights for the fabrication of lightweight, lead-free, and highly efficient wearable shielding materials tailored for the mid-energy radiation range.

2. Materials and methods

2.1. Fabrication of metal oxide-based epoxy resin composites

Bismuth, nickel, and cerium oxide nanoparticles were purchased from Sigma Aldrich and the epoxy resin and its hardener (Methyl Ethyl Ketone Peroxide/MEKP) from Polymer Products (Phils.) Inc. Metal oxides were mixed to epoxy resin at varying concentrations resulting to different densities (Table 1). Composites were prepared using an open mold casting technique [10]. The mixture was poured in a silicon mold with diameter of 14 cm with a maximum height of 1 cm. The nanocomposites were air dried for 24 hrs. to ensure solidification.

Among the metal oxides, bismuth oxide has excellent attenuation properties [21]. It is also good to note that it has good thermal stability and insulating property that can be considered for most applications like radiation protection [22]. Meanwhile, nickel oxide exhibits good mechanical reinforcement due to its hardness and high compressive strength. It also provides thermal conductivity, helping the epoxy resin withstand high temperatures without degradation [23]. While the two nanomaterials have opposing thermal characteristics, cerium oxide was added to neutralize the thermal issues of the two nanomaterials. Cerium oxide offers excellent mechanical reinforcement through its rigidity and scratch resistance. Its thermal properties, including high thermal stability and resistance to oxidation, contribute to the longevity of the epoxy composite under extreme conditions [24].

2.2. Physical characterization of the metal oxide-based epoxy resin nanocomposites

Measurement of densities was carried out via water displacement method and analytical balance with 0.1 g accuracy. The empirical densities were compared to calculated densities using Eq. (1) given by Nanda [25] and Naqvi et al. [26]:

$$\rho_T = \frac{1}{\left(\frac{w_1}{\rho_1}\right) + \left(\frac{w_2}{\rho_2}\right) + \dots + \left(\frac{w_n}{\rho_n}\right)} \quad (1)$$

where ρ_T is the theoretical density and $\frac{w_n}{\rho_n}$ is the ratio of the weight fraction and the density of the material. The assumption to have voids in the composite is highly possible. Therefore, volume fraction of voids (Eq. (2)) can also be calculated using this equation:

$$v_v = \frac{(\rho_T - \rho_E)}{\rho_T} \quad (2)$$

where ρ_E is the empirical density of the composite.

A total of eight thickness measurements were made using the Vernier caliper to obtain the average thickness of the fabricated samples and recorded for the calculation of the mass attenuation coefficient using the experimental values (cf. Fig. 1.A).

The morphological investigation was carried out using Phenom XL tabletop Scanning Electron Microscope (SEM). The Energy Dispersive X-ray (EDX) was incorporated in the SEM which was utilized to analyze the elemental composition of the samples. Five

Table 1
Composite concentration, average thickness, and its densities.

Sample ID	Composition (%)					Density (g/cc)		Volume Fraction	Average Thickness (cm)
	Epoxy Resin	MEKP	Bi ₂ O ₃	CeO ₂	NiO	Average Empirical	Theoretical		
X	97.0	3	0	0	0	1.101	1.144	0.038	0.628
B	95.5	3	1.5	0	0	1.236	1.159	-0.067	0.614
C	95.5	3	0	1.5	0	1.166	1.158	-0.006	0.594
N	95.5	3	0	0	1.5	1.254	1.159	-0.082	0.598
BC	95.5	3	0.75	0.75	0	1.273	1.159	-0.099	0.590
BN	95.5	3	0	0.75	0.75	1.142	1.158	0.014	0.600
CN	95.5	3	0.75	0	0.75	1.118	1.159	0.036	0.595
BCN	95.5	3	0.5	0.5	0.5	1.208	1.159	-0.042	0.614

Table 2
Mid-energy gamma sources.

Source	Nominal Activity (μ Ci)	Reference Date	Half-Life	Gamma Energy (keV)
Na-22	0.1	December 2019	2.6 years	511, 1274
Cs-137	0.1	October 2019	30.07 years	661.7
Mn-54	1.0	December 2019	312.3 days	834.8

different regions from the sample were used as the region of interest. The surface morphology and the elemental compositions were examined to ensure homogeneity of the samples. Additionally, nanoparticle distribution was investigated using Schoolab Compound Microscope with 15x magnification eyepiece and 4/0.1, 160/- objective lens.

2.3. Experimental approach for radiation shielding measurements

Gamma sources were prepared such as Na-22 (2a), Cs-137 (2b), and Mn-54 (2c). The characteristics of the gamma sources were shown in Table 2. A NaI (TI) scintillator (Model 12I12/3, Serial 112223C) of Alpha Spectra, Inc. Scintillation Detectors was utilized in a computer system with Maestro software installed. The detector is placed 2.5–2.7 cm away from the gamma sources (see Fig. 1.C). The working voltage was set to 850 V and the detection time is 3,600 s. Before each measurement per day, a background radiation measurement was implemented. The three natural gamma sources were initially scanned and recorded as the incident radiation intensity (I_0) and the succeeding measurements with the fabricated plates were recorded as the radiation intensity after the shielding (I). Samples are positioned 1.2 cm away from the detector and 1 cm from the source and assigned as x-distance between the source and the detector (cf. Fig. 1.B, C).

The linear attenuation coefficient (μ) or LAC (Eq. (3)) was derived using the Beer-Lambert's Law equation [27]:

$$\mu = -\frac{\ln\left(\frac{I}{I_0}\right)}{x} \quad (3)$$

Given the calculated linear attenuation coefficient, the mass attenuation coefficient (MAC) (Eq. (4)) was calculated as follows [27]:

$$MAC = \frac{\mu}{\rho} \quad (4)$$

where ρ is the material density expressed in g/cm³. Additional parameters including the mean free path (MFP), half value layer (HVL), and tenth value layer (TVL) were calculated using the equations [27]:

$$MFP = \frac{1}{\mu} \quad (5)$$

$$HVL = \frac{\ln 2}{\mu} \quad (6)$$

$$TVL = \frac{\ln 10}{\mu} \quad (7)$$

Mean free path (Eq. (5)) is the minimum distance between particles to interact, while half value layer (Eq. (6)) is the required thickness to decrease the radiation intensity by half, and the tenth value layer (Eq. (7)) is the thickness to decrease the intensity by one-tenth.

2.3.1. Radiation protection efficiency

To further evaluate the effectiveness of the shielding parameters, the radiation protection efficiency (RPE) (Eq. (8)) was calculated using the following equation [28]:

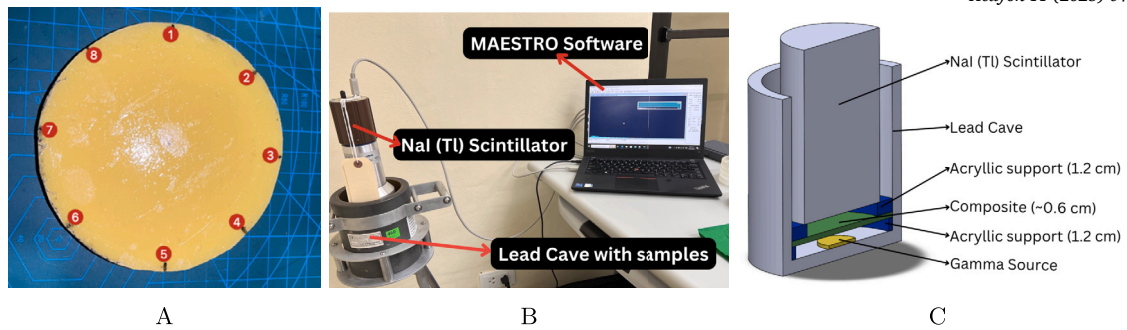


Fig. 1. (A) Fabricated shielding material with corresponding regions of thickness measurements; (B) actual gamma shielding experimental setup; and (C) cross-sectional view of the gamma measurement inside a lead cave.

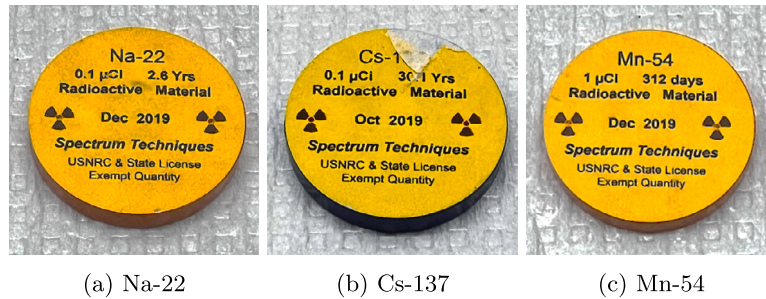


Fig. 2. (A) Na-22, (B) Cs-137, and (C) Mn-54 Gamma sources.

$$RPE(\%) = \left(1 - \frac{I}{I_0}\right) \times 100 \quad (8)$$

where I_0 is the incident radiation intensity and I is the radiation intensity after the shielding was introduced.

3. Results and discussions

3.1. Morphological and elemental analysis

Five different regions were subjected to scanning electron microscopy (SEM) and energy dispersive X-ray (EDX) analyses. Similar morphological structures were observed among the five regions. Each sample was represented in Fig. 3.A-H for its morphological and elemental analyses (cf. Table 3).

Samples with bismuth oxide and nickel oxide exhibited significant observable grains, while samples with cerium oxide showed a more polymeric and wrinkled surface texture. The color gradient in the EDX results mapped the elemental abundance in the regions of interest. Specifically, the orange-colored regions indicated the presence of nickel oxide, which displayed heterogeneity in its distribution.

Among the samples, nickel oxide demonstrated a tendency to agglomerate. This agglomeration can be attributed to several factors, such as molecular and electrostatic interactions, high surface energy, or the effects of solvents during the synthesis of nanomaterials. Additionally, nickel oxide's ferromagnetic properties can further contribute to agglomeration. Structurally, nickel oxide is presumed to have a hexagonal configuration, as referenced from the Materials Project database for NiO (mp-1180047), version v2023.11.1 [29]. Hence, the result from the empirical density calculation to the theoretical density has deviations.

Since the particle distribution cannot be clearly observed using the SEM, Schoolab Compound Microscope was utilized, and images obtained were characterized using ImageJ software. Converting the images based on pixels to the objective lens and eyepiece magnification, the calculated field of view (FOV) in a 15x eyepiece yields 5000 micrometers. Calculating the value to the image width in pixels, which is 1024 pixels, gives approximately 4.88 µm/pixel. All raw images were taken using the 50MP, ISO 2000, and F1.7 camera settings, without post-processing.

Maxima segmented particles were obtained using ImageJ with the following settings: images were converted to 16-bit type, the threshold was adjusted to increase contrast and brightness, and automatic maxima calculation was selected with a prominence set to greater than 10 pixels. The output type was set to segmented particles (Table 4).

Based on Table 4, nickel oxide, among all the nanofillers, has the tendency to agglomerate, as shown in the maxima segmented particles result. Due to its agglomeration, the relative size became so large that it measures 9.699 µm on average. Meanwhile, cerium oxide distributes more evenly on the epoxy resin matrix.

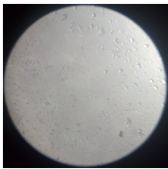
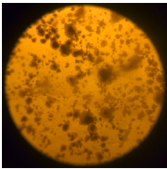
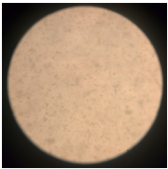
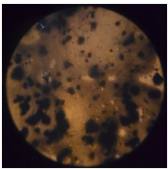
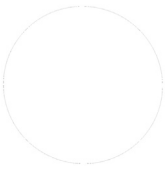
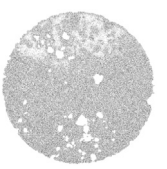

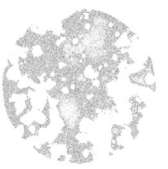
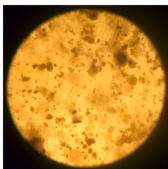
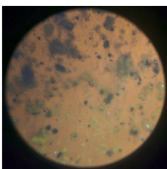
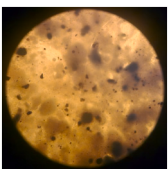
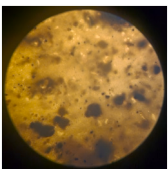

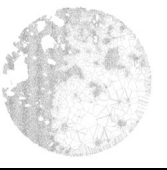
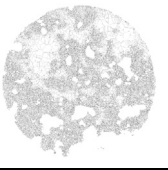
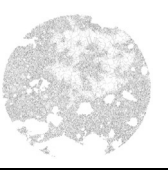
Table 3

Average Elemental Composition using Energy Dispersive X-ray (EDX).

Sample ID	Carbon		Oxygen		Bismuth		Nickel		Cerium	
	Atomic%	Weight%	Atomic%	Weight%	Atomic%	Weight%	Atomic%	Weight%	Atomic%	Weight%
X	58.82	51.75	41.18	48.25	-	-	-	-	-	-
B	68.28	39.39	27.81	21.36	3.91	39.25	-	-	-	-
C	57.81	25.64	30.97	18.28	-	-	-	-	11.23	56.09
N	63.61	49.12	31.48	32.38	-	-	4.90	18.50	-	-
BC	63.52	34.77	31.35	22.84	1.97	12.76	-	-	3.17	29.64
BN	66.72	39.80	23.08	18.34	1.62	16.84	8.58	25.01	-	-
CN	63.03	35.06	20.67	15.32	-	-	14.88	40.46	1.41	9.17
BCN	63.40	32.91	26.88	18.54	3.06	23.24	4.51	11.70	2.16	13.62

Table 4

Optical microscopy of the fabricated composites under the compound microscope at 15x eyepiece and 4/0.1, 160/- objective lens magnification and its relative measurements through ImageJ software.

Sample ID	X	B	C	N
Optical Image				
				
Maxima Segmented Particles				
Total Count	95	6560	47607	3504
Ave. Feret's Diameter (μm)	43.163	5.69	3.358	9.699
Circularity	0.965	0.869	0.88	0.832
Sample ID	BC	BN	CN	BCN
Optical Image				
				
Maxima Segmented Particles				
Total Count	7834	4617	1059	942
Ave. Feret's Diameter (μm)	5.395	6.077	8.557	11.727
Circularity	0.886	0.903	0.911	0.879

As the nanomaterials were combined, nickel oxide causes agglomeration of other nanoparticles, creating heterogeneity in the composite. White portions in the maxima segmented particles represent the accumulation of particles in a particular region. Sample C has the least white portions, which indicates a well-distributed dispersion of the particles on the polymer matrix. Additionally, it has the lowest Feret's diameter measurement at 3.358 μm.

3.2. Radiation shielding evaluation

Samples B, C, BN, and BCN have increasing trends, while X, N, BC, and CN have common highest LAC and MAC for Mn-54 source (cf. Tables 5, 6; Figs. 4, 5). Mn-54 has a faster decay rate than the Na-22 and Cs-137 sources; therefore, data gathering must

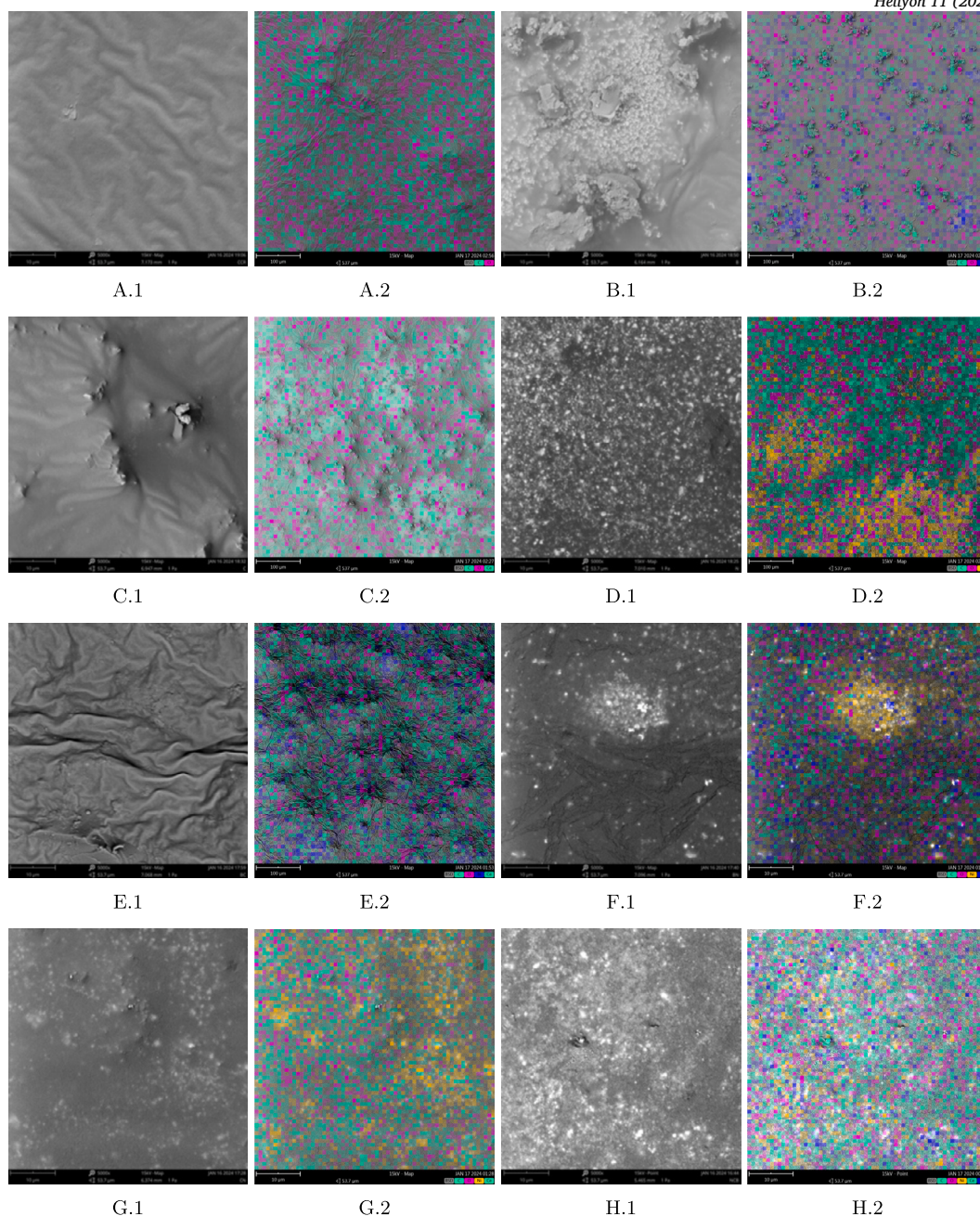


Fig. 3. SEM micrographs (1) and EDX mapping (2) of the samples at 5000x magnification of (A) clear cast resin only, (B) bismuth oxide-polymer, (C) cerium oxide-polymer, (D) nickel oxide-polymer, (E) bismuth-cerium-polymer, (F) bismuth-nickel-polymer, (G) cerium-nickel-polymer, and (H) bismuth-cerium-nickel-polymer.

be conducted in compressed timelines due to the half-life differences. Mass and linear attenuation coefficients of pure lead were calculated using XCOM online database developed by National Institute of Science and Technology [30]. Furthermore, the shorter distance calculated, the more efficient the composite was fabricated. Thereby, similar trends were observed for the Sample B and BC having relatively shorter distances for the particle to interact and thickness of the material to decrease the intensity by half and tenth values among other sample composites for a higher energy range (*cf.* Tables 7–9; Figs. 6–8).

3.3. Factors affecting attenuation coefficient

The present investigation observed an unanticipated trend where the attenuation coefficient of the pristine polymer was greater than that of some sample polymer modified with metal oxides. This discrepancy necessitates a more comprehensive investigation into the fundamental mechanisms influencing the attenuation characteristics. Epoxy resins are commonly utilized as the matrix material

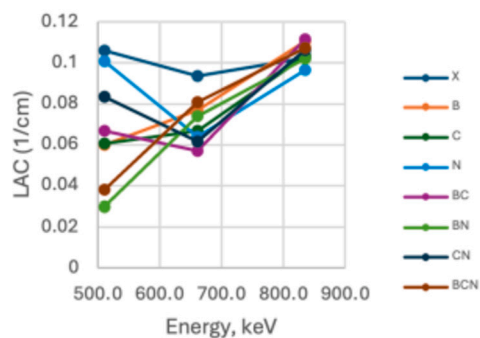


Fig. 4. Linear Attenuation Coefficient (1/cm) vs. Energy (keV) graph

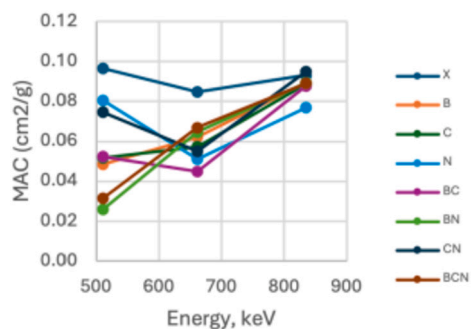


Fig. 5. Mass Attenuation Coefficient (cm²/g) vs. Energy (keV) graph

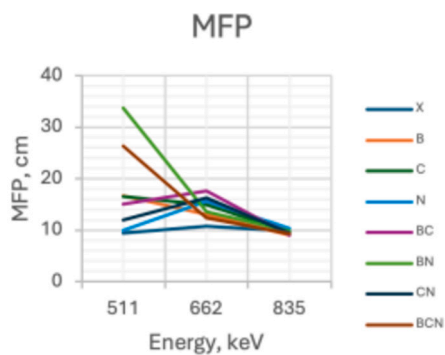


Fig. 6. Mean Free Path (cm) vs. Energy (keV) graph

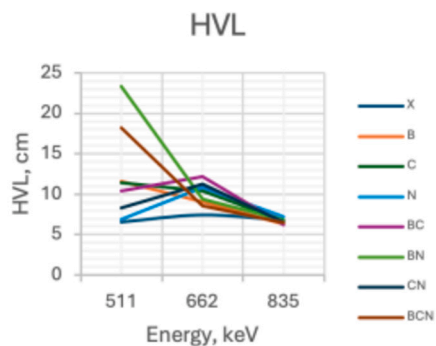


Fig. 7. Half Value Layer (cm) vs. Energy (keV) graph

Table 5
Linear Attenuation Coefficient (1/cm)

	511 keV	661.7 keV	834.8 keV
X	0.1061877	0.0935062	0.1025276
B	0.0598595	0.0768715	0.1106563
C	0.0604869	0.0668159	0.1033679
N	0.1009088	0.0639440	0.0964299
BC	0.0666838	0.0569462	0.1117897
BN	0.0296730	0.0738414	0.1020424
CN	0.0834073	0.0614856	0.1062835
BCN	0.0380228	0.0808438	0.1074110
Pb	1.830755	1.25077	0.9623665

Table 6
Mass Attenuation Coefficient (cm²/g)

	511 keV	661.7 keV	834.8 keV
X	0.0964499	0.0849313	0.0931254
B	0.0484215	0.0621829	0.0895120
C	0.0518821	0.0573108	0.0886629
N	0.0804615	0.0509869	0.0768902
BC	0.0523799	0.0447310	0.0878104
BN	0.0259874	0.0646698	0.0893681
CN	0.0746358	0.0550195	0.0951063
BCN	0.0314834	0.0669398	0.0889378
Pb	0.1613000	0.1102000	0.0847900

Table 7
Mean Free Path (cm)

	511 keV	661.7 keV	834.8 keV
X	9.41728	10.69447	9.75347
B	16.70579	13.00872	9.03699
C	16.53250	14.96650	9.67419
N	9.90994	15.63869	10.37023
BC	14.99615	17.56045	8.94537
BN	33.70070	13.54254	9.79985
CN	11.98936	16.26397	9.40879
BCN	26.30002	12.36954	9.31003

Table 8
Half Value Layer (cm)

Sample ID	511 keV	661.7 keV	834.8 keV
X	6.52618	7.41127	6.75915
B	11.57711	9.01504	6.26264
C	11.45702	10.37178	6.70421
N	6.86759	10.83761	7.18657
BC	10.39233	12.16939	6.19914
BN	23.35459	9.38498	6.79130
CN	8.30862	11.27093	6.52029
BCN	18.22591	8.57209	6.45185

Table 9
Tenth Value Layer (cm)

Sample ID	511 keV	661.7 keV	834.8 keV
X	21.68409	24.62494	22.45819
B	38.46650	29.95368	20.80845
C	38.06750	34.46163	22.27564
N	22.81848	36.00940	23.87834
BC	34.52991	40.43443	20.59747
BN	77.59874	31.18286	22.56499
CN	27.60651	37.44918	21.66455
BCN	60.55803	28.48191	21.43714

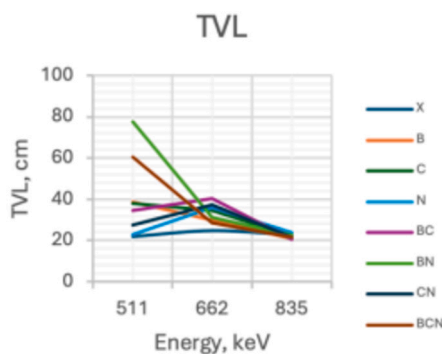


Fig. 8. Tenth Value Layer (cm) vs. Energy (keV) graph

Table 10
Radiation Protection Efficiency (%).

	Na-22	Cs-137	Mn-54
X	6.44986	5.70200	6.23463
B	3.60937	4.61117	6.56991
C	3.52768	3.88953	5.95292
N	5.85945	3.75397	5.60681
BC	3.85555	3.30194	6.37886
BN	1.76535	4.33554	5.94128
CN	4.83962	3.59080	6.12557
BCN	2.30570	4.83878	6.37724

in radiation shielding composites due to their favorable mechanical, thermal, and chemical properties. However, the homogenous incorporation of high-density metal oxide fillers is crucial to enhance the radiation shielding performance.

Based on the results, there are three possible reasons affecting the attenuation coefficient: (1) dispersion and distribution of metal oxides, (2) photon interaction mechanisms, and (3) experimental conditions. The tendency of the nanoparticle to agglomerate during the mixing process creates localization of attenuation (see also Table 4). This agglomeration can be attributed to the molecular and electrostatic interactions, high energy, or solvent during the synthesis. Therefore, uniformity of nanofillers is crucial in radiation shielding. Additionally, uniform thickness is also a factor to be considered for the distribution of the photon interacting with the sample (*c.f.* Table 1). Due to viscosity of the mixture, the thickness across the sample has slight difference. The sample easily hardens as it was casted into the silicon mold. Also, air trapped during casting can also be a consideration in the distribution of particles and thickness. Another factor is the photon interaction in the composite. A more uniform distribution of nanoparticles typically results in more effective gamma attenuation, as it enhances photon interaction consistently across the material, compared to agglomerated and unevenly distributed nanoparticles, which can lead to varying and often lower attenuation coefficients. Additionally, the intrinsic properties of the polymer matrix and the metal oxides might result in unexpected interaction patterns. Voids in the composite may add up factor since air has different density which creates a more complex system for the interaction. The third factor is the experimental condition. The radiation energy levels of the check sources and their respective interaction probabilities with the composite materials might vary as well. Different time of testing per sample incurs greater chance of variation in the result due to the half-life of the gamma sources. Most importantly, the significance of collimating the gamma sources to control the radiation intensity and photon interaction would be beneficial to gather consistent data (*cf.* Fig. 1.B). Detector is exposed widely to the gamma source which allows randomness of the photon direction [31].

3.4. Radiation protection efficiency

The Radiation Protection Efficiency (RPE) results for the different composites when exposed to Na-22, Cs-137, and Mn-54 gamma sources are presented in Table 10. The results showed good performance for Mn-54. Composite with bismuth oxide yields the highest efficiency which can be attributed to its heavier atomic nuclei and total density. With the intermediate performance of around 5-6% RPE, it can still make a significant difference in various practical applications such as protection in medical imaging and therapy [32], therapeutic radiology for targeted cancer cell treatment [32], [33], industrial radiography for inspecting welds and materials, environmental monitoring, radiation laboratory experiments and demonstrations, and worker protection in nuclear powerplants [33].

4. Conclusion

This study aimed to develop and evaluate lead-free epoxy resin nanocomposites incorporating bismuth oxide, nickel oxide, and cerium oxide for effective mid-energy radiation protection. The findings revealed that pure epoxy resin exhibited higher attenuation

coefficients compared to the modified composites, an observation that underscores the complexities involved in the incorporation and dispersion of metal oxides within a polymer matrix.

The detailed morphological and elemental analyses indicated significant agglomeration tendencies of the metal oxide, particularly nickel oxide, leading to non-uniform distribution and reduced shielding effectiveness. The study highlighted the crucial role of homogeneity and the need for optimized dispersion techniques to achieve consistent and improved radiation attenuation properties.

Despite the very high performance of lead as a standard shielding material, epoxy resin, B, BC, CN, and BCN samples provided better mass attenuation coefficients with values of 0.103, 0.111, 0.112, 0.106, and 0.107 cm²/g, respectively. Given that the concentration of the nanoparticles incorporated is at 1.5% w/v, increasing the concentration will likely yield higher attenuation capabilities.

Radiation Protection Efficiency (RPE) measurements demonstrated that while the composites showed varying degrees of effectiveness, pure epoxy resin consistently performed better with an RPE of around 6% across different radiation sources. Despite the modest RPE values for pure epoxy resin, samples B, BC, and BCN outperformed epoxy resin for higher energy radiation with values of 6.570, 6.379, and 6.377%, respectively. These materials have potential practical applications in various fields, including medical imaging, industrial radiography, environmental monitoring, and nuclear power plant worker protection. Incorporating similar metamaterials and varying fabrication designs can achieve the desired attenuation for specific applications. Note that attenuation can be modulated by varying the cross-sectional distance and density of the attenuating material.

Future research should focus on addressing the challenges of nanoparticle dispersion and agglomeration to enhance the radiation shielding performance of polymer-based composites. Additionally, exploring alternative synthesis methods and composite formulations could lead to more effective and reliable materials for radiation protection.

Overall, this study contributes valuable insights into the design and development of lead-free radiation shielding materials, emphasizing the importance of uniform nanoparticle distribution and the need for further optimization to fully realize their potential in practical applications.

CRediT authorship contribution statement

Toni Beth Guatato-Lopez: Writing – review & editing, Writing – original draft, Visualization, Validation, Software, Resources, Project administration, Methodology, Investigation, Formal analysis, Data curation, Conceptualization. **Alvie Asuncion-Astronomo:** Writing – review & editing, Validation, Supervision, Software, Resources, Methodology, Investigation, Formal analysis, Data curation, Conceptualization. **Gil Nonato C. Santos:** Writing – review & editing, Supervision, Resources, Project administration, Investigation, Conceptualization.

Use of artificial intelligence

During the preparation of this work, the author TBG Lopez used ChatGPT to check grammar, tenses consistency, and flow of discussion. After using this tool, the author reviewed and edited the content as needed and takes full responsibility for the content of the publication.

Funding

This research received support from the Department of Science and Technology – PCIEERD, PNRI, and De La Salle University.

Declaration of competing interest

The authors declare the following financial interests/personal relationships which may be considered as potential competing interests: Toni Beth Guatato-Lopez reports financial support was provided by Republic of the Philippines Department of Science and Technology. Gil Nonato C. Santos reports article publishing charges was provided by De La Salle University. If there are other authors, they declare that they have no known competing financial interests or personal relationships that could have appeared to influence the work reported in this paper.

Acknowledgement

The authors would like to express their gratitude to Mr. Nico Ricci Lopez for providing the compound microscope, to Engr. Emmanuel Arriola for the CAD model of the experimental setup, and Mr. James Harold Cabalhug for the LaTeX formatting assistance.

Data and Code Availability Statement

Data will be made available on request.

References

- [1] K. Jakubczyk, K. Dec, J. Kałduńska, D. Kawczuga, J. Kochman, K. Janda, Reactive oxygen species - sources, functions, oxidative damage, *Pol. Merkur. Lek.* 48 (284) (Apr. 2020) 124–127.

- [2] R.B. Ravelli, S.M. McSweeney, The 'fingerprint' that x-rays can leave on structures, *Structure* 8 (3) (Mar. 2000) 315–328.
- [3] B. Wu, Y. Wei, F.-Q. Liu, Q. Zhang, C.-B. Wang, H. Bai, Biological effects of low dose x-irradiation on human bone marrow mesenchymal stem cells, *Zhongguo Shi Yan Xue Ye Xue Za Zhi* 19 (5) (Oct. 2011) 1214–1217.
- [4] M.J. Thompson, et al., Patient-centred outcomes of imaging tests: recommendations for patients, clinicians and researchers, *BMJ Qual. Saf.* 32 (9) (Sep. 2023) 536–545.
- [5] N. Moonkum, C. Pilapong, K. Daowtak, G. Tochaikul, Radiation protection device composite of epoxy resin and iodine contrast media for low-dose radiation protection in diagnostic radiology, *Polymers (Basel)* 15 (2) (Jan. 2023) 430.
- [6] D.B. Richardson, et al., Cancer mortality after low dose exposure to ionising radiation in workers in France, the United Kingdom, and the United States (INWORKS): cohort study, *BMJ* 382 (Aug. 2023) e074520.
- [7] W.J. Lee, et al., Projected lifetime cancer risks from occupational radiation exposure among diagnostic medical radiation workers in South Korea, *BMC Cancer* 18 (1) (Dec. 2018) 1206.
- [8] S. Yonai, Radiation protection, in: *Advances in Accelerators and Medical Physics*, Elsevier, 2023, pp. 185–192, chapter 16.
- [9] Z. Li, W. Zhou, X. Zhang, Y. Gao, S. Guo, High-efficiency, flexibility and lead-free x-ray shielding multilayered polymer composites: layered structure design and shielding mechanism, *Sci. Rep.* 11 (1) (Feb. 2021) 4384.
- [10] N.J. AbuAlRoos, N.A. Baharul Amin, R. Zainon, Conventional and new lead-free radiation shielding materials for radiation protection in nuclear medicine: a review, *Radiat. Phys. Chem.* 165 (Dec. 2019) 108439.
- [11] A. Navas-Acien, E. Guallar, E.K. Silbergeld, S.J. Rothenberg, Lead exposure and cardiovascular disease—a systematic review, *Environ. Health Perspect.* 115 (3) (Mar. 2007) 472–482.
- [12] L.-T. Allan-Blitz, C. Goldfine, T.B. Erickson, Environmental and health risks posed to children by artisanal gold mining: a systematic review, *SAGE Open Med.* 10 (Jan. 2022) 205031212210769.
- [13] P.G. Ghule, G.T. Bholane, R.P. Joshi, S.S. Dahiwal, P.N. Shelke, S.D. Dhole, Gamma radiation shielding properties of unsaturated polyester /bi2o3 composites: an experimental, theoretical and simulation approach, *Radiat. Phys. Chem.* 216 (Mar. 2024) 111452.
- [14] E. Toto, L. Lambertini, S. Laurenzi, M.G. Santonicola, Recent advances and challenges in polymer-based materials for space radiation shielding, *Polymers (Basel)* 16 (3) (Jan. 2024) 382.
- [15] A.H. Almuqrin, D.A. Aloraini, M.I. Abualsayed, Epoxy-reinforced heavy metal oxides for gamma ray shielding purposes, *Open Chem.* 21 (1) (May 2023).
- [16] Y. Karabul, O. İçelli, The assessment of usage of epoxy based micro and nano-structured composites enriched with bi2o3 and wo3 particles for radiation shielding, *Results Phys.* 26 (Jul. 2021) 104423.
- [17] M. Almurayshid, S. Alsagabi, Y. Alssalim, Z. Alotaibi, R. Almsalam, Feasibility of polymer-based composite materials as radiation shield, *Radiat. Phys. Chem.* 183 (Jun. 2021) 109425.
- [18] K.V. Sathish, et al., X-rays/gamma rays radiation shielding properties of barium-nickel-iron oxide nanocomposite synthesized via low temperature solution combustion method, *Radiat. Phys. Chem.* 194 (May 2022) 110053.
- [19] H.M. Almutairi, W.M. Al-Saleh, M.I. Abualsayed, M. Elsaifi, Effect of cerium (iv) oxide particle size on polydimethylsiloxane polymer to form flexible materials against ionizing radiation, *Polymers (Basel)* 15 (13) (Jun. 2023) 2883.
- [20] S. Alshahri, et al., Ldpe/bismuth oxide nanocomposite: preparation, characterization and application in x-ray shielding, *Polymers (Basel)* 13 (18) (Sep. 2021) 3081.
- [21] B.M. Chandrika, et al., Synthesis, physical, optical and radiation shielding properties of barium-bismuth oxide borate-a novel nanomaterial, *Nucl. Eng. Technol.* 55 (5) (May 2023) 1783–1790.
- [22] H.M.H. Zakaly, et al., Decoding the role of bismuth oxide in advancing structural, thermal, and nuclear properties of [b2o3–li2o–sio2]–nb2o5 glass systems, *Radiat. Phys. Chem.* 223 (Oct. 2024) 111984.
- [23] A.K. Gupta, et al., Advances in nickel-containing high-entropy alloys: from fundamentals to additive manufacturing, *Materials* 17 (15) (Aug. 2024) 3826.
- [24] D. Yılmaz, B. Aktaş, Ş. Yalçın, M. Albaşkara, Erbium oxide and cerium oxide-doped borosilicate glasses as radiation shielding material, *Radiat. Eff. Defects Solids* 175 (5–6) (May 2020) 458–471.
- [25] B.P. Nanda, A. Satapathy, Processing and characterization of epoxy composites reinforced with short human hair, *IOP Conf. Ser., Mater. Sci. Eng.* 178 (Feb. 2017) 012012.
- [26] S.Z. Naqvi, J. Ramkumar, K.K. Kar, Fly ash/glass fiber/carbon fiber-reinforced thermoset composites, in: *Handbook of Fly Ash*, Elsevier, 2022, pp. 373–400.
- [27] S.B. Kolavekar, G.B. Hiremath, P.N. Patil, N.M. Badiger, N.H. Ayachit, Investigation of gamma-ray shielding parameters of bismuth phospho-tellurite glasses doped with varying sm2o3, *Heliyon* 8 (11) (Nov. 2022) e11788.
- [28] G. AlMisned, et al., Enhancement of gamma-ray shielding properties in cobalt-doped heavy metal borate glasses: the role of lanthanum oxide reinforcement, *Materials* 14 (24) (Dec. 2021) 7703.
- [29] A. Jain, et al., Commentary: the materials project: a materials genome approach to accelerating materials innovation, *APL Mater.* 1 (1) (Jul. 2013).
- [30] M.J. Berger, et al., Xcom: Photon cross sections database, NIST Standard Reference Database 8 (XGAM), 2023.
- [31] G.R. Gilmore, *Practical Gamma-Ray Spectrometry*, Wiley, 2008.
- [32] M. Mahesh, *The essential physics of medical imaging*, third edition, *Med. Phys.* 40 (7) (Jul. 2013).
- [33] *Radiation protection and safety of radiation sources: International basic safety standards*, 2014.